Azis et al. Nanoscale Research Letters (2018) 13:160
https://doi.org/10.1186/s11671-018-2562-x

Nanoscale Research Letters

NANO EXPRESS Open Access

Influence of pH Adjustment Parameter for Sol–Gel Modification on Structural, Microstructure, and Magnetic Properties of Nanocrystalline Strontium Ferrite

Raba'ah Syahidah Azis[1,2*], Sakinah Sulaiman[1], Idza Riati Ibrahim[1,2], Azmi Zakaria[1,2], Jumiah Hassan[1,2], Nor Nadhirah Che Muda[1], Rodziah Nazlan[3], Norlaily M. Saiden[2], Yap Wing Fen[1,2], Muhammad Syazwan Mustaffa[1,2] and Khamirul Amin Matori[1,2]

Abstract

Synthesis of nanocrystalline strontium ferrite ($SrFe_{12}O_{19}$) via sol–gel is sensitive to its modification parameters. Therefore, in this study, an attempt of regulating the pH as a sol–gel modification parameter during preparation of $SrFe_{12}O_{19}$ nanoparticles sintered at a low sintering temperature of 900 °C has been presented. The relationship of varying pH (pH 0 to 8) on structural, microstructures, and magnetic behaviors of $SrFe_{12}O_{19}$ nanoparticles were characterized by X-ray diffraction (XRD), field emission scanning microscope (FESEM), and vibrating sample magnetometer (VSM). Varying the pH of precursor exhibited a strong effect on the sintered density, crystal structure and magnetic properties of the $SrFe_{12}O_{19}$ nanoparticles. As the pH is 0, the $SrFe_{12}O_{19}$ produced relatively largest density, saturation magnetization, M_s, and coercivity, H_c, at a low sintering temperature of 900 °C. The grain size of $SrFe_{12}O_{19}$ is obtained in the range of 73.6 to 133.3 nm. The porosity of the sample affected the density and the magnetic properties of the $SrFe_{12}O_{19}$ ferrite. It is suggested that the low-temperature sintered $SrFe_{12}O_{19}$ at pH 0 displayed M_s of 44.19 emu/g and H_c of 6403.6 Oe, possessing a significant potential for applying in low-temperature co-fired ceramic permanent magnet.

Keywords: Sol–gel, pH, Structural, Microstructure, Magnetic behavior, Strontium hexaferrite ($SrFe_{12}O_{19}$)

Highlight

- Synthesis of strontium ferrite ($SrFe_{12}O_{19}$) nanoparticles using sol–gel auto combustion technique.
- The $SrFe_{12}O_{19}$ nanoferrite phase was obtained at a low sintering temperature, 900 °C.
- Magnetic parameter of saturation magnetization M_s, remnant M_r, and coercivity H_c decrease as pH increases.

Background

Strontium ferrite ($SrFe_{12}O_{19}$) has been extensively studied for their potential applications in microwave devices, high-density magnetic recording, electronic devices, and permanent magnet. Permanent magnet ferrites are widely used in the electrical manufacturing industry due to its several advantages [1] and impressive properties such as high electrical resistivity [2], large hysteresis loss, and high intrinsic coercivity [3]. It is best known as a good heat resistance and corrosion resistance and useful for many applications. Strontium ferrite has attracted more scientific studies in recent years due to its high magnetic anisotropy, which is responsible for the high coercivity of crystalline structure [4, 5] and thus can ensure a high coercivity even when the size of the particles is reduced into nanoscale with single-domain structure. The ferromagnetism exhibited by $SrFe_{12}O_{19}$ is attributed

* Correspondence: rabaah@upm.edu.my
[1]Institute of Advanced Technology, Universiti Putra Malaysia, 43400 UPM Serdang, Selangor, Malaysia
[2]Departments of Physics, Faculty of Science, Universiti Putra Malaysia, 43400 UPM Serdang, Selangor, Malaysia
Full list of author information is available at the end of the article

to the Fe^{3+} ion sublattices present in the structure. They are distributed in three octahedral (12 k, 2a, $4f_2$), one tetrahedral ($4f_1$), and one bipyramidal sites (2b). From these sites, 12 k, 2a, and 2b are represented as the high spin states and $4f_1$ and $4f_2$ are considered as the low spin states [6, 7]. The magnetic moments of the Fe^{3+} ions are coupled to each other by super-exchange interactions mediated by O^{2-} ions. The Sr^{2+} ion is responsible for the large magnetic uniaxial anisotropy as it causes a perturbation of the crystal lattice [8]. Strontium hexaferrite ($SrFe_{12}O_{19}$) nanoparticles have a mean particle size of less than 0.1 μm and are made of homogeneous particle size distribution [9]. The smaller particle size produces a large surface area, significantly enhancing the $SrFe_{12}O_{19}$ nanoparticles properties, such as its chemical, physical, mechanical, and magnetic properties, resulting in interesting properties for nanoferrite applications.

The conventional ceramic solid-state method is difficult in obtaining nanoparticles and mono-sized particles [4, 5]. It has limitations such as long heating schedule at high sintering temperature of about 1300 °C, higher obtained grain/particle size, and higher time consumption. The experimental conditions involved in the making of the ferrite nanoparticles play a key role in the resulting properties as well as the particle size of the ferrite nanoparticles. In order to achieve highly homogeneous $SrFe_{12}O_{19}$ nanoparticles consisting of a single-domain structure at low sintering or calcination temperature, various methods have been introduced so that a wide grain size distribution with anomolous grain growth promoted during sintering could be avoided. The methods include co-precipitation [9, 10], salt-melt method [11], hydrothermal [12, 13], microemulsion [14], and sol–gel process [1, 4, 15]. Among these methods, sol–gel route is a low-cost, simple, and reliable method to control the stoichiometry and to produce nanocrystalline ferrite. The sol–gel process produces a homogeneous mixed oxide that can lower the calcination temperature and produce a smaller crystallite size [3]. Optimizing the molar ratio of Fe to Sr (Fe/Sr) is very important to produce a single-phase sample, ultrafine particle, and lower calcination temperatures [1]. This ratio varies with change in starting materials and with change in method of production [1]. At high calcination temperature, both grain size and exchange coupling increase. These will be unfavorable for getting a good quality of permanent magnet [16]. In general, metal alkoxides are often used as raw materials in sol–gel process, but many of the alkoxides are very difficult to be obtained and dealt with because of the high sensitivity to the atmospheric moisture. Moreover, it is not easy to control the rate of alkoxide hydrolysis when multi-component ceramics are to be prepared. Metal salts are employed in this study since they are very useful, cheaper, and easier to handle. Besides, metal salts can be dissolved in many kinds of organic solvents, thus forming metal complexes by chelating the metal ions with organic ligands [17]. There are several sol–gel modification processes have been reported, such as pH adjustment [1, 18], basic agent [3], surfactant [1], carboxylic acid [2], and starting metal salts [3], to reduce the final calcination temperature, crystallite size [2], and high anisotropy of $SrFe_{12}O_{19}$ nanoparticles [12]. In sol–gel methods, the ability to form hydroxides and/or oxides strongly depends on the pH of the solution and the charge/radius ratio of the metal cation [17]. Furthermore, the pH of sol controls the amount of H^+ or OH^- ions in the sol that effectively determines the polymerization of the metal–oxygen bonds. Also, it is known that during the sol–gel process, complexing process with citric acid is sensitive to pH values [19, 20]. Therefore, homogeneity of the sol which is essential for phase formation would be determined by the pH of the solution. It is well known that the magnetic properties of $SrFe_{12}O_{19}$ are strongly dependent on its morphology, particle/grain size, shape, orientation, and domain configurations by modifying the synthesis parameters. Therefore, in this work, we intend to regulate the pH of the solution as a sol–gel modification parameter to produce nanocrystalline ferrite with considerable values of magnetic properties at a lower calcination temperature.

Methods

The experimental sequences of this study consisted of two major stages which were the synthesis of strontium ferrite nanoparticles via the sol–gel method (the "Synthesis of Strontium Ferrite Nanoparticles" section) and were followed by the characterizations of structural, microstructure, and magnetic properties of prepared strontium ferrite (the "Characterizations of Strontium Ferrite" section).

Synthesis of Strontium Ferrite Nanoparticles

Strontium ferrite nanoparticles have been synthesized via the sol–gel method. In this method, strontium nitrate anhydrous granular $Sr(NO_3)_2$ (98%, Alfa Aeser), iron(III) nitrate $Fe(NO_3)_3$ (99%, HmbG), citric acid $C_3H_4(OH)(COOH)_3$ (99%, Alfa Aeser), ammonia NH_4OH (25%, SYSTERM), and deionized water were used as starting materials for the preparation of the sample. Appropriate amounts of $Sr(NO_3)_2$ and $Fe(NO_3)_3$ are dissolved in 100 ml of deionized water for a few minutes at 60 °C with a constant stirrer rotation of 250 rpm to make an aqueous solution. Citric acid was added as a chelating agent with molar ratio of citrate to nitrate (C/N = 0.75), and the temperature was raised to 80 °C. The mixtures were continuously

stirred, and NH_4OH was added in order to vary the pH from pH 0 to pH 8. The pH was measured by HI2211 pH/ORP meter (HANNA instruments). The solutions were continuously stirred and heated for several hours at 90 °C, and the solution slowly turned into green sticky gel. Upon the formation of a dense sticky gel, the temperature of the hot plate is then increased up to 200 °C and combusted the gels for an hour for the dehydration process. The obtained powders were calcined at 900 °C for 6 h with the heating rate of 5 °C/min. A step-wise description of the synthesis procedure of $SrFe_{12}O_{19}$ nanoparticles is shown in Fig. 1.

Characterizations of Strontium Ferrite

Characterization measurement of strontium ferrite has been carried out in terms of its structural, microstructure, and magnetic properties. The detailed explanation is shown in the following subsections.

Structural Properties

The structural characterization of the samples was characterized by X-ray diffraction (XRD) technique using a Philips X'pert X-Ray Diffractometer Model 7602 EA Almelo with Cu Kα radiation at 1.5418 Å. The range of diffraction angle used is from 20° to 80° at room temperature. The accelerating current and working voltage were 35 mA and 4.0 kV respectively. The data were analyzed by using an X'Pert High Score Plus software.

Fourier transform infrared (FTIR) characterization was carried out by a Perkin Elmer Fourier transform infrared spectrometer model 1650 to determine the infrared spectrum of absorption and emission bands of the

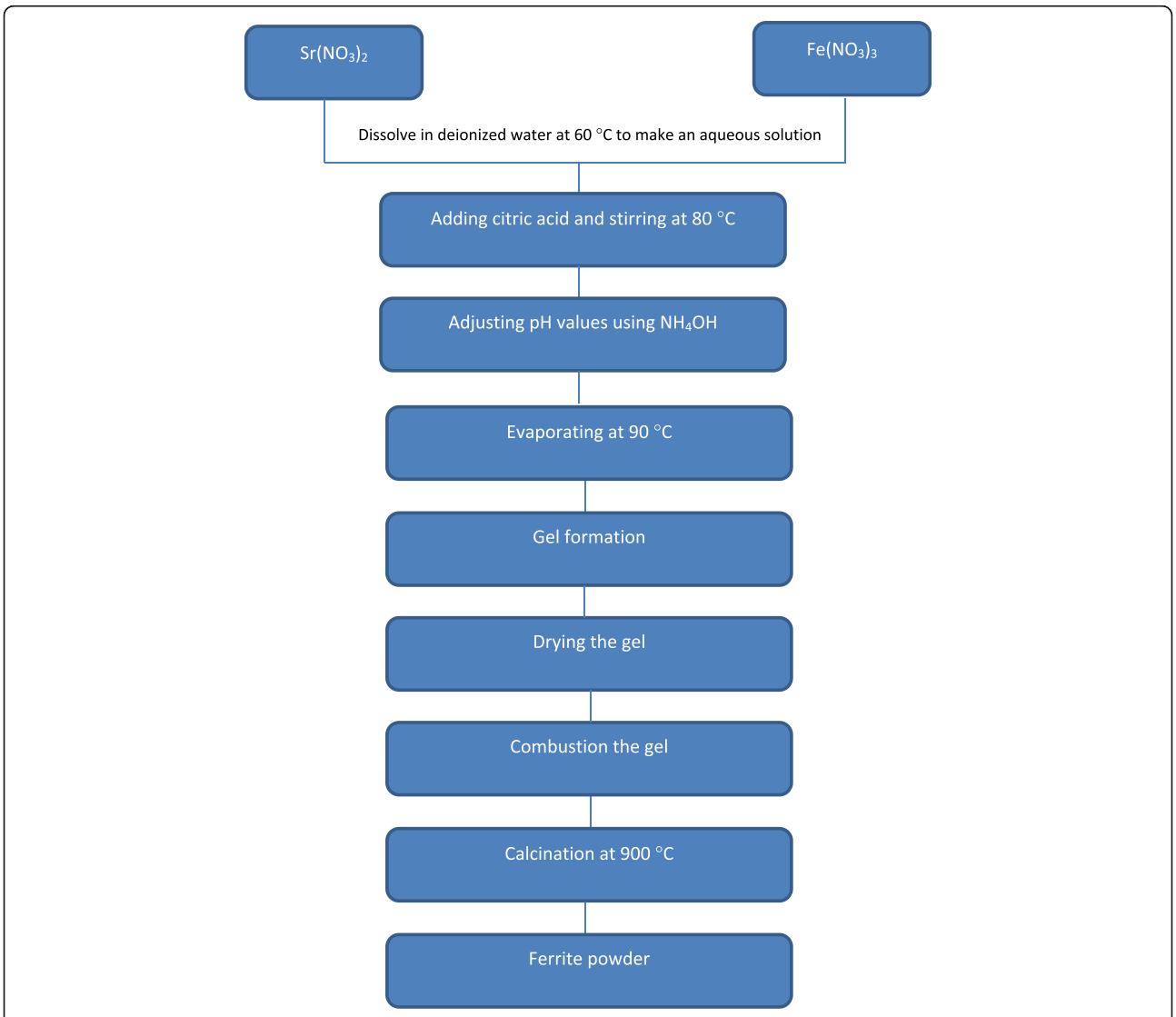

Fig. 1 Flowchart for preparing $SrFe_{12}O_{19}$ nanoparticles powders by sol–gel method

sample. It was performed between infrared spectra of 280–4000 cm^{-1}.

Microstructure Properties

The microstructural observation was performed by a field emission scanning electron microscope (FESEM) using a FEI Nova NanoSEM 230 machine. The distribution of grain size image was fixed at a magnification of 100kx with 5.0 kV accelerating voltage. The distributions of grain sizes were obtained by taking 200 different grain images for the sample and estimating the mean diameters of individual grains by using the imageJ software. The grain size distribution was measured by a mean linear intercept method.

Density

The density was measured using a Hildebrand Densitometer Model H-300 S. The density of the sintered pellet was obtained using the Archimedes principle with water as the fluid medium by Eq. 1,

$$\rho_{\text{exp}} = \left(\frac{W_{\text{air}} - W_{\text{water}}}{W_{\text{water}}}\right) \times \rho_w \tag{1}$$

ρ_{exp} is the measured sample's density, ρ_w is the density of water, W_{air} is the sample's weight in air, and W_{water} is the sample's weight in water.

Magnetic Properties

The magnetic properties of samples were measured by a vibrating sample magnetometer (VSM) Model 7404 LakeShore. The measurement was carried out at room temperature. The 12 kOe external field was applied parallel to the sample.

Results and Discussion

Structural Analysis

Figure 2 shows the X-ray diffraction (XRD) spectra of $SrFe_{12}O_{19}$ nanocrystalline by varying the pH. The structure of XRD peaks was referred to standard $SrFe_{12}O_{19}$ with JCPDS reference code of 98-004-3603. The characteristic peaks and miller indices of $SrFe_{12}O_{19}$ are also shown in the figure. The highest intensity can be observed at 2θ (34.218°) with miller indices of [1 1 4]. The formation of single-phase $SrFe_{12}O_{19}$ was obtained at relatively low calcination temperature of 900 °C. There were no observed peaks corresponding to some of the reagent precursors or other secondary phases and intermediate products, except for the sample prepared at pH 8 where a minute amount of hematite Fe_2O_3 phase was detected and all of the samples have a good crystallinity as shown in the figure. The formation of secondary Fe_2O_3 phase observed for sample prepared at pH 8 had reduced the purity of $SrFe_{12}O_{19}$ to 87.8%. The Fe_2O_3 patterns were indexed to ICSD reference code of 98-004-1067. The presence of Fe_2O_3 phase is due to insufficient calcination temperature for the sample prepared at

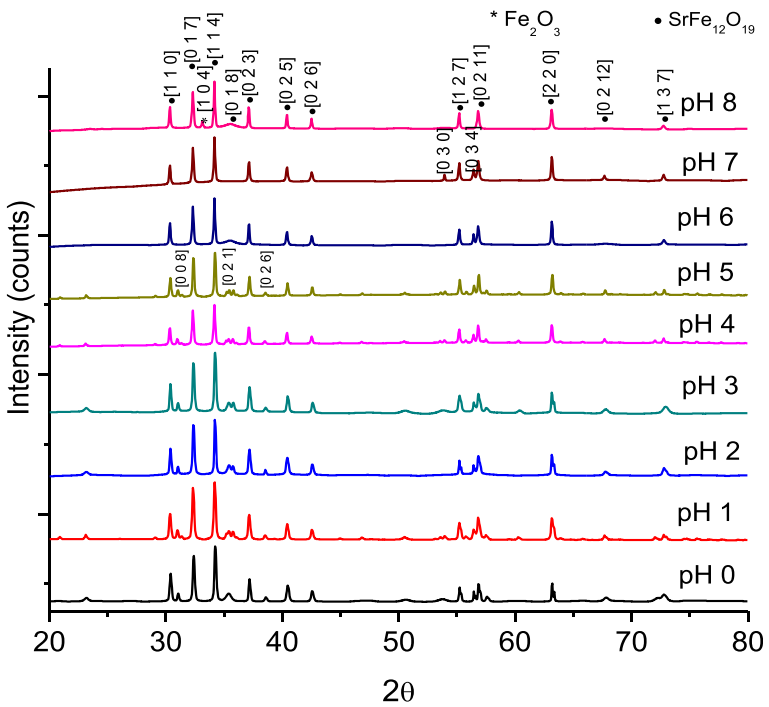

Fig. 2 The X-ray diffraction spectra of $SrFe_{12}O_{19}$ for pH 0 to pH 8, sintered at 900 °C

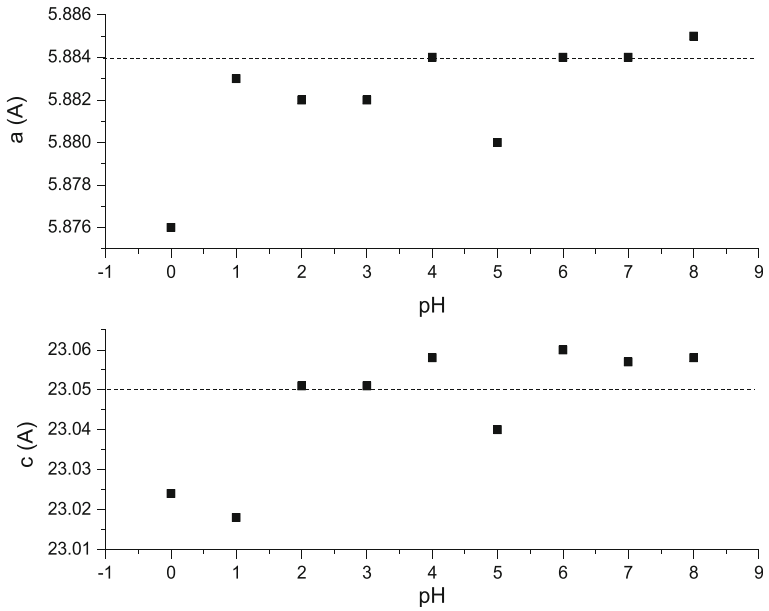

Fig. 3 The lattice parameters *a* and *c* of $SrFe_{12}O_{19}$ nanoparticles for pH 0 to pH 8, sintered at 900 °C. The dash lines are the reference values of the lattice parameters *a* and *c*

pH 8 [21]. It was found that high acidity in medium solution from pH 0 to 3 favored the formation of high crystallinity $SrFe_{12}O_{19}$ phase. The increasing pH of the sol assisted the formation of negatively charged iron gels and the adsorption of positively charged Sr ions on iron gels. Consequently, more homogeneous solution was obtained, and it results in the easy formation of $SrFe_{12}O_{19}$ phase [3]. Even though the formation of $SrFe_{12}O_{19}$ is easier with increased pH, heterogeneous ceramic aggregates could be formed due to localized shifts in the immediate vicinity of the complex undergoing polymerization [22]. Therefore, crystalline growth might be inhibited, therefore reducing the crystallinity from pH 4 onwards. This was shown by the increase of XRD peak intensity by the improvement of the crystallinity of $SrFe_{12}O_{19}$ prepared using pH 1 to pH 3, however slowly decreased with increased pH values from 4 to 8. The formation of crystalline $SrFe_{12}O_{19}$ after being calcined at 900 °C is attributed to the higher degree of compositional homogeneity as well as the greater heat

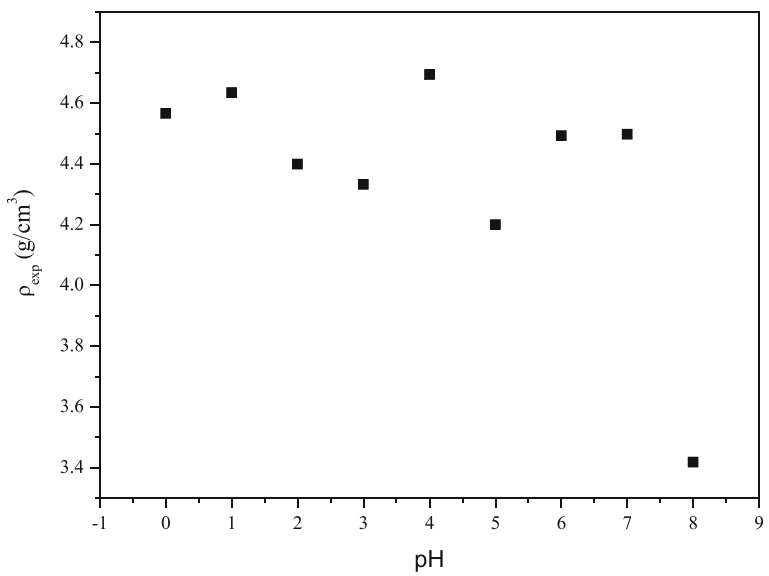

Fig. 4 Experimental density of $SrFe_{12}O_{19}$ nanoparticles for pH 0 to pH 8, sintered at 900 °C

Table 1 The structural, microstructural, and magnetic parameters of the $SrFe_{12}O_{19}$ sintered at 900 °C

pH	Peak pos. 2θ (°)	Miller indices (hkl)	Peak width (°)	Space group	Lattice constant		V_{cell} (nm^3)	ρ_{xrd} (gcm^{-3})	ρ_{exp} (gcm^{-3})	P (%)	M_s (emu/g)	M_r (emu/g)	M_s (emu/cm^3)	M_r/M_s	H_c (Oe)	Grain size (nm)
					a (Å)	c (Å)										
0	34.32	[114]	0.19	P63/mmc	5.876	23.024	0.689	5.12	4.566	10.7	44.188	27.713	226.243	0.627	6403.6	74
1	34.20	[114]	0.13	P63/mmc	5.883	23.018	0.690	5.11	4.634	9.5	4.776	3.001	24.405	0.628	6094.7	108
2	34.21	[114]	0.13	P63/mmc	5.882	23.051	0.691	5.11	4.399	13.9	7.822	4.870	39.970	0.623	6005.8	114
3	34.22	[114]	0.16	P63/mmc	5.882	23.051	0.691	5.11	3.832	24.9	2.168	1.373	11.078	0.633	5966.1	115
4	34.20	[114]	0.16	P63/mmc	5.884	23.058	0.691	5.10	4.693	8.1	3.006	1.929	15.330	0.642	5808.6	96
5	34.25	[114]	0.16	P63/mmc	5.880	23.040	0.689	5.11	4.200	17.6	2.016	1.309	10.301	0.649	6074.8	111
6	34.18	[114]	0.16	P63/mmc	5.884	23.060	0.691	5.10	4.492	12.1	7.022	4.416	35.812	0.629	5377.0	120
7	34.18	[114]	0.18	P63/mmc	5.884	23.057	0.691	5.10	4.497	11.8	4.028	2.554	20.542	0.634	5461.2	116
8	34.17	[114]	0.18	P63/mmc	5.885	23.058	0.691	5.10	3.419	32.9	2.975	1.934	15.172	0.650	5117.7	133

generated from the exothermic reaction of nitrates and citric acid [21].

The lattice parameter a and c value observed were not far different compared to the theoretical $SrFe_{12}O_{19}$ lattice constant where $a = 5.8820$ Å and $c = 23.0230$ Å [23] (Fig. 3). The a and c parameters observed are similar to those in Masoudpanah et al. [3] and Dang et al. [12]. The volume cell V_{cell} and density of XRD ρ_{xrd} used in this study depend on the crystallographic parameter which have a hexagonal crystal system with space group of *P63/mmc*. The V_{cell} were calculated using Eq. (2);

$$V_{cell} = \frac{\sqrt{3}}{2} a^2 c \tag{2}$$

where a and c are the lattice constant. The theoretical density ρ_{theory} of sample was calculated using Eq. (3),

$$\rho_{theory} = \frac{2M}{N_A V} \tag{3}$$

where M is the molecular weight of $SrFe_{12}O_{19}$ which equals to 1061.765 g. The weight of two molecules in one unit cell is $2 \times 1061.765 = 2123.53$ g; N_A is the Avogadro's number (6.022×10^{23} mol^{-1}).

The porosity P of the samples can be calculated using Eq. (4);

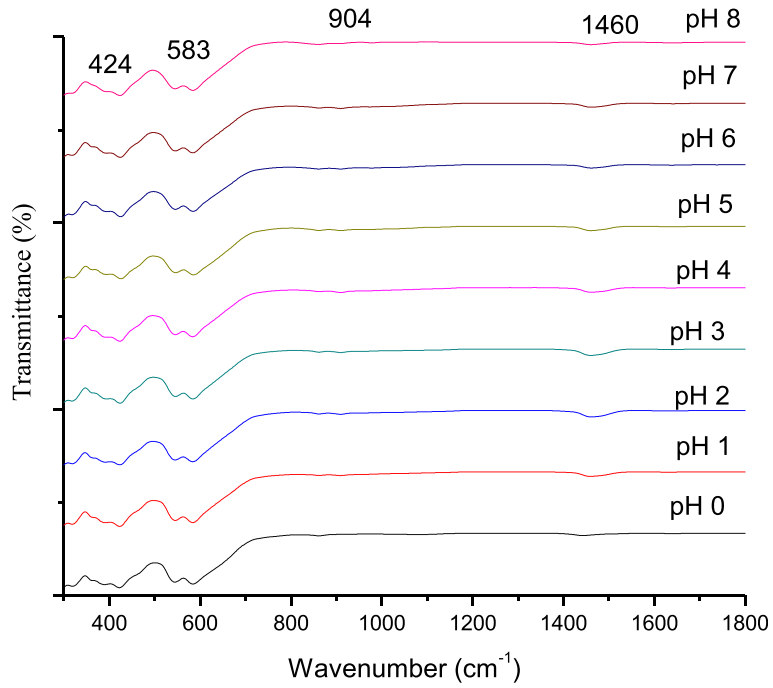

Fig. 5 The FTIR spectra of $SrFe_{12}O_{19}$ for pH 0 to pH 8, sintered at 900 °C

$$P = \left(\frac{1-\rho_{\text{exp}}}{\rho_{\text{theory}}}\right) \times 100\% \quad (4)$$

As the pH value increased, the experimental density of the samples ρ_{exp} was decreased except for some fluctuations observed for samples prepared at pH 4, 6, and 7 with optimum value of experimental density and less porosity obtained for sample prepared at pH 4. The optimum density and porosity were recorded as 4.693 g/cm^3 and 8.15% respectively (Fig. 4, Table 1). The X-ray density shown in Table 1 is greater than the experimental density which may be due to the presence of pores created during the sintering process. The porous feature of agglomerates is also attributed to the liberation of a large amount of gas such as NH_3 during the combustion process [24].

The FTIR spectra of sintered $SrFe_{12}O_{19}$ at varying pH from pH 0 to pH 8 are shown in Fig. 5. The FTIR spectra of a precursor noticeably appeared in the range of 430, 583, 904, and 1446 cm^{-1} of IR characteristic bands. The absorption band at 436 cm^{-1} was indicated as a stretching band of CH_2, proving the presence of CH saturated

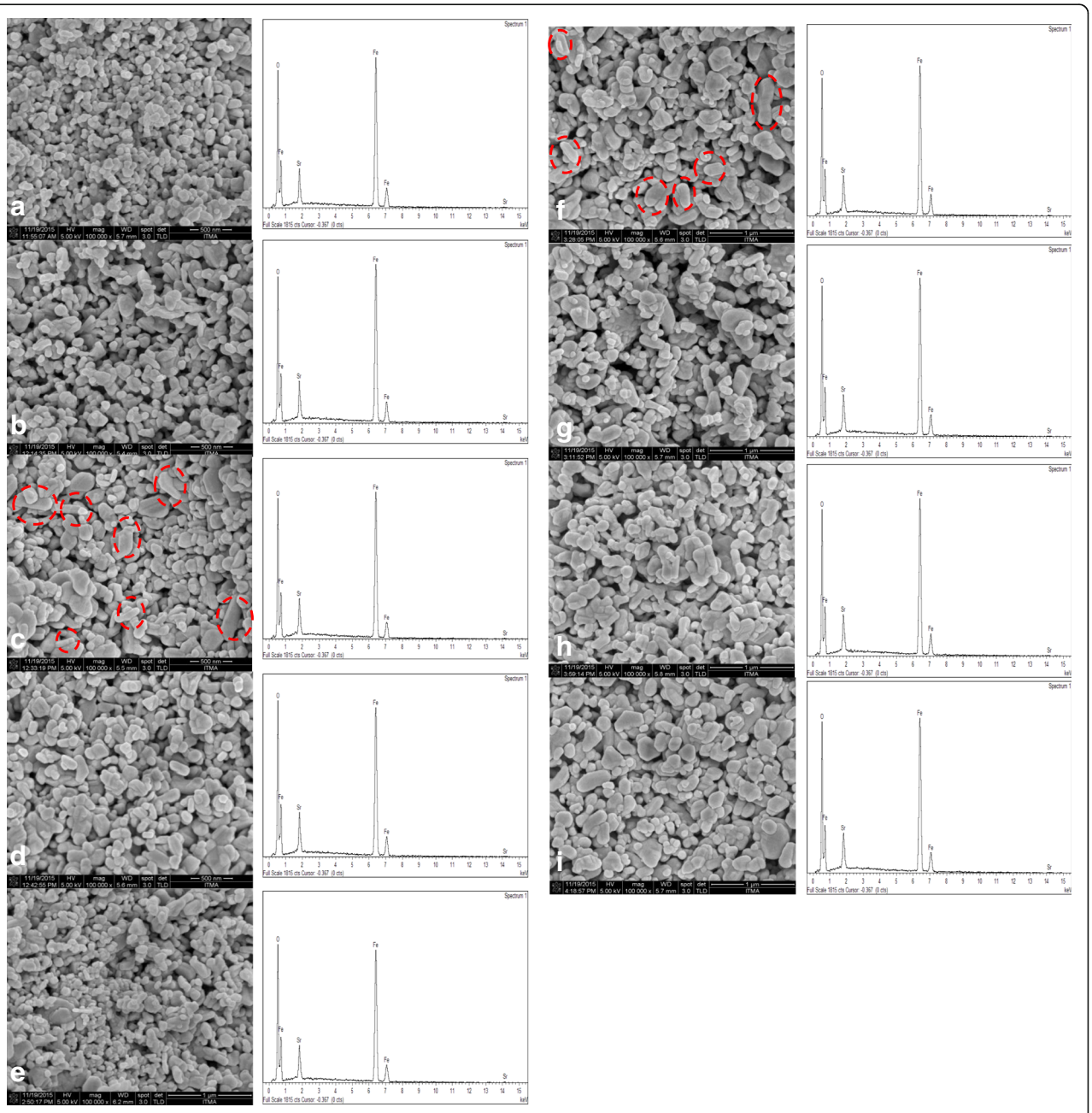

Fig. 6 The FESEM micrographs of samples sintered at 900 °C by varying pH: **a** pH 0, **b** pH 1, **c** pH 2, **d** pH 3, **e** pH 4, **f** pH 5, **g** pH 6, **h** pH 7, and **i** pH 8

compound [25]. Bands at 583 cm^{-1} show the characteristic metal oxygen vibration Sr–O Fe–O [20]. The absorption bands of range 443–600 cm^{-1} were ascribed to the formation of strontium ferrite as stretching vibration of metal–oxygen bond [26–29]. This confirms that, the $SrFe_{12}O_{19}$ was formed at a sintering temperature of 900 °C. The relatively strong and broad bands at peaks 904 cm^{-1} revealed that there was an amine functional group for N–H vibration due to the decomposition of NH_3. Meanwhile, Pereira et al. [29] also stated that a broad vibration of Sr–O stretching indicate the formation of strontium nanoferrite. The absorption band at 1446 cm^{-1} indicates the vibrating bands of Fe–O–Fe bands due to the decomposition of metal with oxides band [25].

Microstructural Analysis

The microstructure images of bulk $SrFe_{12}O_{19}$ and the EDX spectra are shown in Fig. 6, while the grain size distributions of samples are shown in Fig. 7. The average grain sizes were found in the range of 73.6 to 133.3 nm. The average grain size of the samples does not show large variation except for samples with pH 4 and pH 8. The grain sizes were agglomerated as increasing the pH value. A relatively small and packed grain size with an average of 73.6 nm and narrowest grain size distribution among all was observed for pH 0. The grain size increased with increased pH values from pH 0 to pH 3, decreased at pH 4, and further increased until pH 8. The results are in agreement with the XRD spectra as shown in Fig. 2 that the degree of crystallinity reduced for

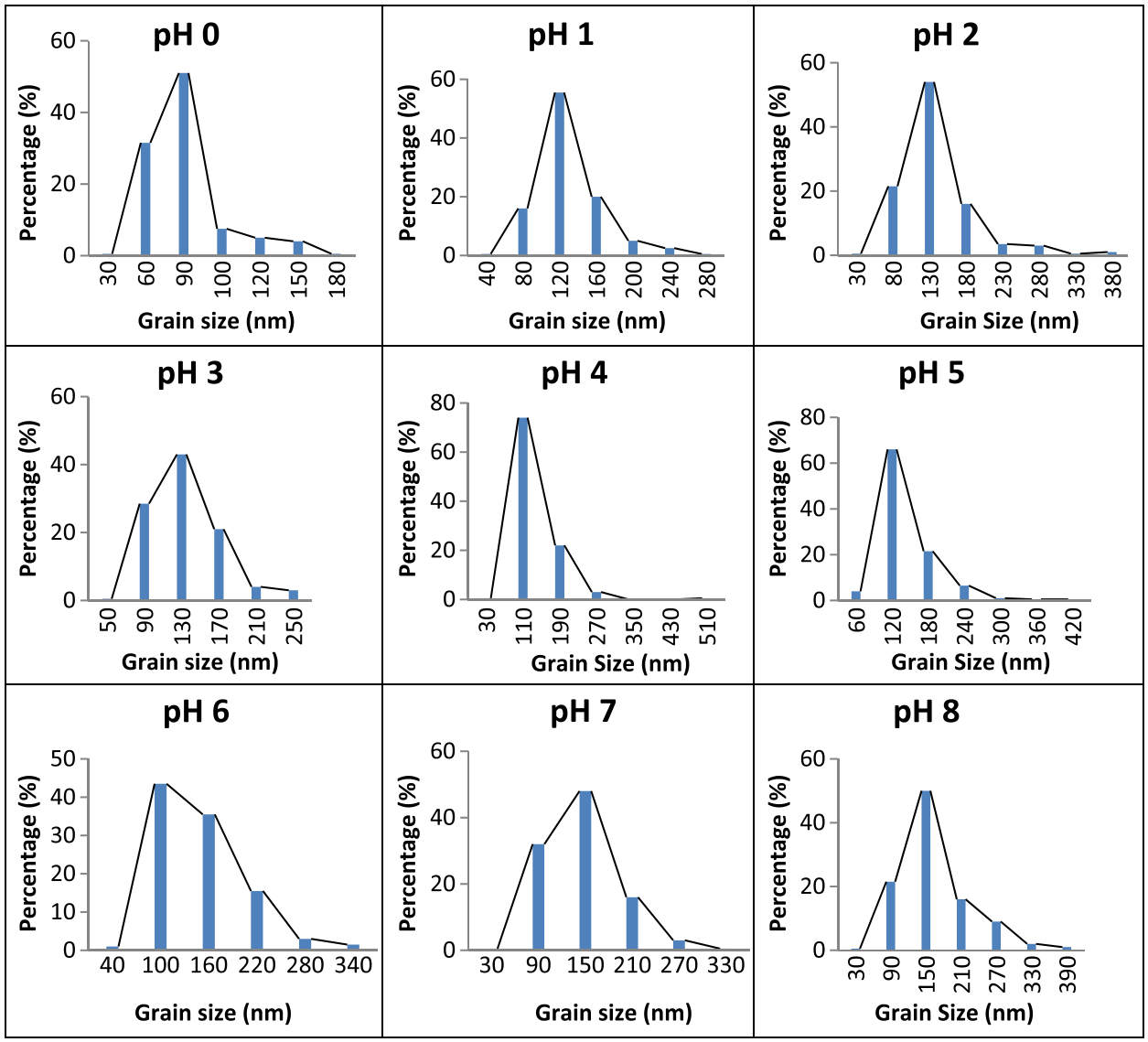

Fig. 7 Grain size distribution for $SrFe_{12}O_{19}$ calcined at 900 °C by varying pH: **a** pH 0, **b** pH 1, **c** pH 2, **d** pH 3, **e** pH 4, **f** pH 5, **g** pH 6, **h** pH 7, and **i** pH 8

sample at pH 4. From Fig. 6e, for sample prepared at pH 4, it shows that the grains are not homogeneously distributed and not uniformly formed.

The finest grain size exhibited highest M_s, M_r, and H_c. The grains for samples having pH 0 were spherical in shape and in contact with another grain to form a necking structure. The contact was obvious with increase in pH values, thus showing a more elongated grain structure. The grain size/shape distributions became larger and non-uniform as the pH values increased. The histogram of the grain size distribution shifted from small grain sizes to exhibiting larger grain sizes. The increased combustion rate and heat released from reaction may also increase the crystallite size [30]. The red dotted lines in the histogram (Fig. 7) marked the average grain size of the sample. The microstructure showed some of the samples exhibited large porosity due to the presence of polyvinyl alcohol during preparation of bulk $SrFe_{12}O_{19}$ nanoferrite in pellet form as well as the liberation of gas during sample preparation.

Magnetic Behaviors

The development of *M–H* hysteresis loop at various pH is illustrated in Fig. 8. A further confirmation of this evolution can be seen from the variation of saturation magnetization, M_s, remanence, M_r, squareness ratio, M_r/M_s, and coercivity, H_c, as a function of pH tabulated in Table 1. Magnetization per unit mass is not directly related to the microstructure of the sample; therefore, magnetization per unit volume has been calculated by multiplying the magnetization per unit mass with the experimental density, ρ_{exp}. The M_s, M_r, and H_c are found to be generally decreased with increasing pH by addition of ammonia in a sol–gel precursor. The decrement of magnetic parameters as pH increases could be due to the existence of large amount of diamagnetic phases of ammonia NH_3. It seems that the main effect of the diamagnetic NH_3 are to isolate Sr-ferrite nanoparticles from each other, thus reducing exchange interaction between them and are known to have a detrimental effect on M_s and M_r. As seen previously in the "Microstructural analysis" section, the microstructure of $SrFe_{12}O_{19}$ was affected by increasing the pH value. This is in agreement with the findings reported by Yang et al. [31], where the particles became larger [32] with the increase of pH from 5 to 11. The larger particles were highly affected by strong magnetic interaction between magnetic atoms of Fe in the grains [33].

The *M–H* hysteresis loops in Fig. 8 have been scrutinized, and three significant groups of hysteresis loops characterized by the shapes and values of differentiated group could be observed. The first group consisted majority of the prepared samples which are samples prepared using pH 1, 3, 4, 5, 7, and 8. This group corresponded to the weak ferromagnetic properties with low values of M_s and M_r. It is known that

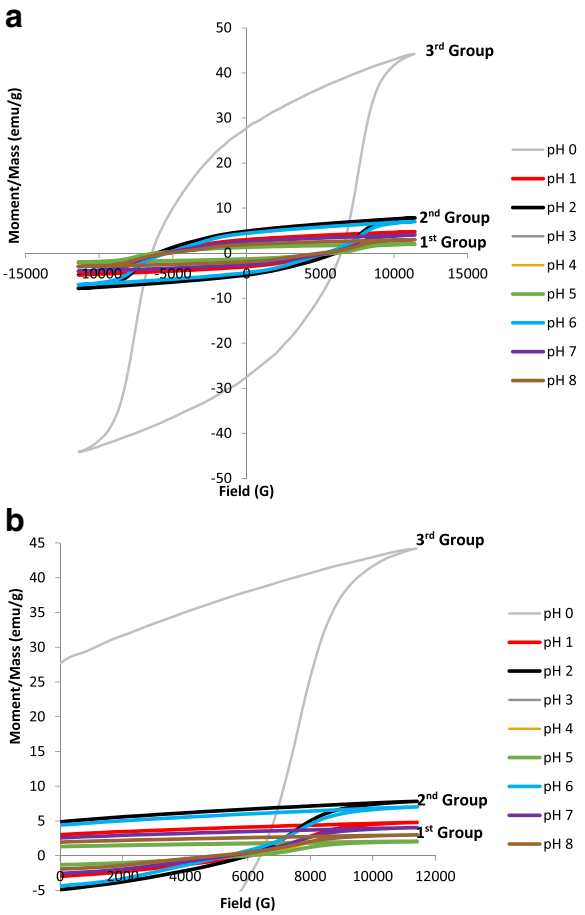

Fig. 8 The *M–H* hysteresis loops of $SrFe_{12}O_{19}$ for **a** pH 0 to pH 8 and **b** close-up graph, varying pH sintered at 900 °C

M_s is particularly depending on the crystallinity of the sample. This could be seen in the samples prepared using pH 4, 5, 7, and 8, where the crystallinity was reduced for the samples, thus displaying lower values of M_s. Furthermore, the presence of 28.2% α-Fe_2O_3 impurity as a secondary phase was detected in sample prepared using pH 8, reducing the crystallinity of the sample and consequently reducing the M_s value. Even though the observed XRD spectra in Fig. 2 displayed high degree of crystallinity for samples prepared using pH 3, the resulting low magnetic property values might be subjected to decrease in density (see Table 1) due to the presence of pores, thus affecting the coercivity in the sample. Since M_s is related to H_c as shown in Eq. (5) [34], the M_s decreased when the H_c increased.

$$H_c = \frac{2K_1}{M_s} \tag{5}$$

It is also known that porosity affects the magnetization process because pores work as a generator of demagnetizing field [35].

It is noticeable that pH 2 and pH 6 fell in the second group in which the samples have moderate hysteresis parameters (Fig. 8). The samples in this group exhibited similar shape of hysteresis loop with the first group but with slightly higher values of M_s and M_r. The H_c values recorded for the samples prepared using pH 2 and pH 6 were 6005.8 and 5377.0 Oe respectively. The M_s values for pH 2 and pH 6 were observed as 7.8 emu/g (226.2 emu/cm^3) and 7.0 emu/g (35.8 emu/cm^3), respectively, whereas the M_r values for pH 2 and pH 6 were given as 4.9 emu/g and 4.4 emu/g respectively. Even though larger grain size was present in the samples, the recorded values were still low since the presence of elongated grains was detected (see the red dotted circles in Fig. 6c, g) in the samples prepared using pH 2 and 6. Since it is known that total anisotropy energy barrier depends on volume and surface anisotropy energy densities, so for a given volume of a particle, the surface area is more for elongated shape particles. Hence, the major contribution from surface to the effective anisotropy and an increase in H_c is also expected in elongated particles [36], thus reducing the M_s.

The third group was detected in an only sample prepared using pH 0. Significant gap was observed between the second and the third groups, indicating the changing properties in samples within this group particularly in the M_s values. Hysteresis loop for pH 0 has the largest M_s, M_r, and H_c with the significant values of 44.19 emu/

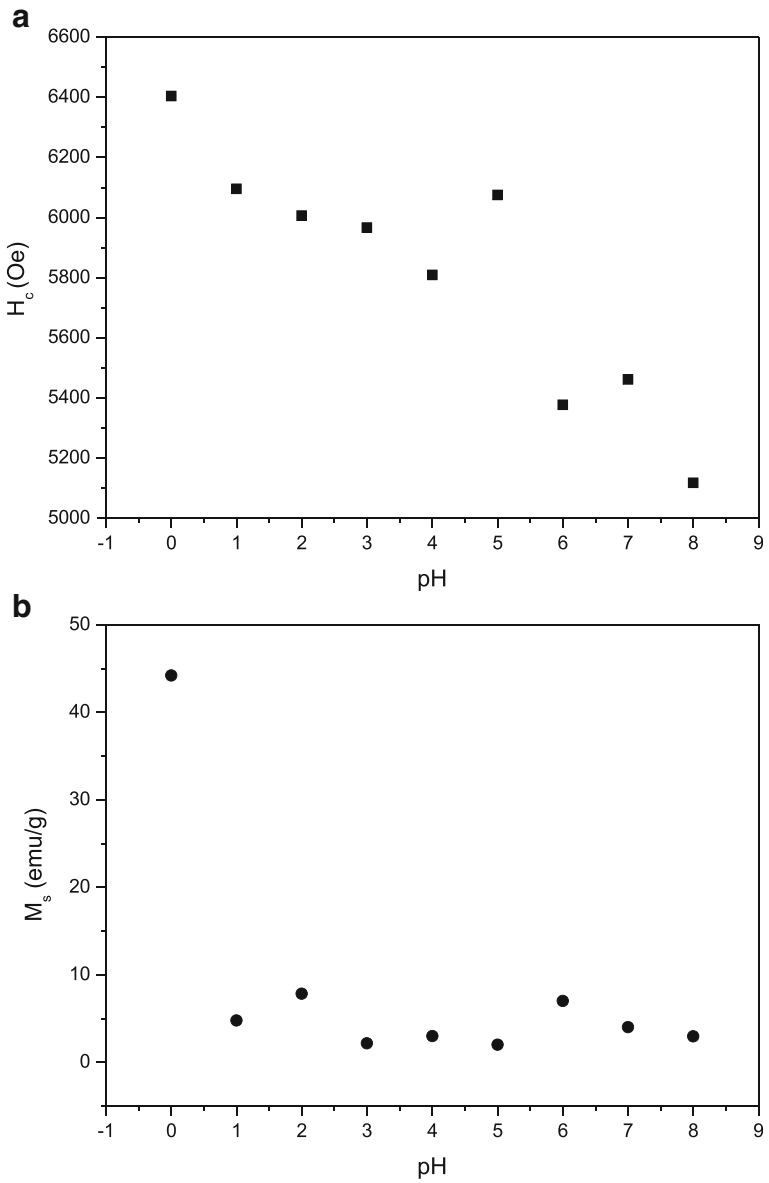

Fig. 9 **a** H_c and **b** M_s of $SrFe_{12}O_{19}$ at varied pH sintered at 900 °C

g (226.2 emu/cm^3), 27.59 emu/g, and 6403.6 Oe respectively. Generally, the M_s values for $SrFe_{12}O_{19}$ could be ranged from 74 to 92 emu/g which are often measured in a single crystal form [8]. The value of M_s for sample prepared using pH 0 was relatively lower than the given values and also with previously reported studies which were 56 emu/g [37] and 53 emu/g [38], both synthesis via the sol–gel method. It is expected that the value of M_s in this study would be increased with further increment of sintering temperatures. However, the H_c value showed a relatively higher value than previous studies which were 5000 Oe [37] and 5200 Oe [38], and according to Pullar [8], no precise value is given for H_c as it varies too much with processing methods and grain size. Meanwhile, no significant difference of M_r was seen as has been previously reported which was 30 emu/g [38]. An obvious erect, larger, and well-defined hysteresis loops could be observed. It is due to the strong ferromagnetic behavior, resulting from the formation of high volume fraction of the complete crystalline $SrFe_{12}O_{19}$ phase as seen in Fig. 2. Thus, a strong interaction of magnetic moments within domains occurred due to exchange forces. This observed phenomenon can be considered as an ordered magnetism in the sample. In fact, in order to obtain an ordered magnetism and a well-formed M–H hysteresis loop, there must exist a significant domain formation, a sufficiently strong anisotropy field, H_a, and optional addition contributions which come from defects such as grain boundaries and pores [39]. It is interesting to note that the broad loops in this group means substantial magnetic storage; thus, the samples possess characteristics which may be useful for practical applications [40].

The H_c variation in Figs. 9a and 10 should deserve some mention: The H_c is observed to generally reduce as pH increased. The decrease in H_c with increasing pH can be attributed to decrement of magnetocrystalline anisotropy with anisotropic Fe^{2+} ions locating on a 2a site and the enlargement of the grain size and is evident in FESEM micrographs (Fig. 6). Furthermore, at pH 8, the coercivity H_c which is 5117.7 Oe was recorded due to the presence of 28.2% α-Fe_2O_3 impurity (Fig. 2). The decrease in H_c was due to the presence of impurity α-Fe_2O_3 which affected the crystalline and grain boundary since it has been reported that the H_c could be affected by important parameters such as particle size, ion substitution, morphology, interface structure, crystal defects, magnetocrystalline anisotropy, and strain [41]. The squareness ratio, M_r/M_s, is calculated from the magnetic data and tabulated in Table 1. Generally, a large M_r/M_s value is preferred in many applications such as magnetic recording media of high density and permanent magnet [42]. The calculated M_r/M_s in this study was found to be in the range of 0.63 to 0.65, indicating that all the samples are predominantly in single magnetic domain structure [43]. M_r/M_s equal to or above 0.5 indicates that the particles are in the single magnetic domain and below 0.5 may be attributed to the formation of multidomain structure [43, 44].

Conclusions

Single-phase nanoparticles of $SrFe_2O_{19}$ prepared using different pH were successfully synthesized by sol–gel method. The effects of structural, microstructural, and magnetic behavior of $SrFe_2O_{19}$ were studied by modifying the pH values at the fix sintering temperature of 900 °C. From this study, it can be concluded that pH values play

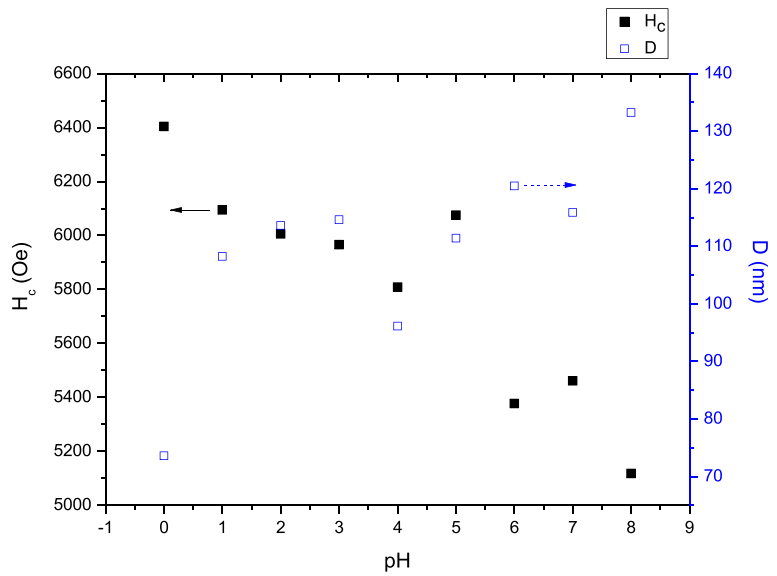

Fig. 10 Relation of H_c and grain size of $SrFe_{12}O_{19}$ at varied pH sintered at 900 °C

an important role in the formation of single-phase $SrFe_{12}O_{19}$ which required pH not more than 7 and, by increasing pH from 0 to 3, the formation of $SrFe_{12}O_{19}$ is favored. SEM micrographs exhibited a circular crystal type of $SrFe_2O_{19}$ with average grain size in the range of 73 to 133 nm. The single-phase $SrFe_2O_{19}$ with optimum magnetic properties are observed in sample prepared at pH 0 which displayed best in-plane saturation magnetization of 44.188 emu/g and remnant magnetization of 27.593 emu/g and with high coercivity of 6403.6 Oe.

Abbreviations

ρ_{exp}: Measured sample's density; ρ_{theory}: Theoretical density; ρ_w: Density of water; ρ_{xrd}: Density of XRD; a: Lattice parameter; C: Carbon; c: Lattice parameter; C/N: Citrate to nitrate; $C_3H_4(OH)(COOH)_3$: Citric acid; EDX: Energy-dispersive X-ray; Fe: Iron; $Fe(NO_3)_3$: Iron(III) nitrate; Fe_2O_3: Hematite; FESEM: Field emission scanning microscope; FTIR: Fourier transform infrared; H: Hydrogen; H_a: Anisotropy field; H_c: Coercivity; IR: Infrared; K_1: Anisotropy constant; M: Molecular weight; M_r: Remanence; M_r/M_s: Squareness ratio; M_s: Saturation magnetization; N: Nitrogen; N_A: Avogadro's number; NH_3: Ammonia; NH_4OH: Ammonia; O: Oxygen; P: Porosity; Sr: Strontium; $Sr(NO_3)_2$: Strontium nitrate anhydrous granular; $SrFe_{12}O_{19}$: Strontium ferrite; V_{cell}: Volume cell; VSM: Vibrating sample magnetometer; W_{air}: Sample's weight in air; W_{water}: Sample's weight in water; XRD: X-ray diffraction

Acknowledgements

The authors would like to thank the Ministry of Education Malaysia for providing funds; MyBrain15, Research University Grants Vot Nos. 9533300, 9541600, and 5524942; and the Department of Physics and the Materials Synthesis and Characterization Laboratories (MSCL) ITMA, UPM, for the measurement facilities.

Funding

The authors would like to thank the Ministry of Education Malaysia for providing funds and MyBrain15, Research University Grants Vot Nos. 9533300, 9541600, and 5524942.

Availability of Data and Materials

The datasets supporting the conclusions of this article are included within the article.

Authors' Contributions

All authors have contributed to the final manuscript of the present investigation. RSA and SS have defined the research topic. RSA, SS, and NNCM are involved in the synthesis, characterization, and analysis of the study. RSA, SS, IRI, and RN wrote the manuscript. AZ, JH, NMS, YWF, MSM, and KAM provided suggestions on the draft of the manuscript. All authors examined and approved the final manuscript.

Competing Interests

The authors declare that they have no competing interests.

Publisher's Note

Author details

[1]Institute of Advanced Technology, Universiti Putra Malaysia, 43400 UPM Serdang, Selangor, Malaysia. [2]Departments of Physics, Faculty of Science, Universiti Putra Malaysia, 43400 UPM Serdang, Selangor, Malaysia. [3]Faculty of Industrial Sciences & Technology, Universiti Malaysia Pahang, Lebuhraya Tun Razak, Gambang, 26300 Kuantan, Malaysia.

Received: 15 February 2018 Accepted: 30 April 2018
Published online: 23 May 2018

References

1. Alamolhoda S, Seyyed Ebrahimi SA, Badiei A (2016) A study on the formation of strontium hexaferrite nanopowder by a sol-gel auto-combustion method in the presence of surfactant. J Magn Mag Mater 303(1):69–72 Elsevier.
2. Masoudpanah SM, Ebrahimi SAS, Ong CK (2012) Journal of magnetism and magnetic materials preparation of strontium hexaferrite film by pulsed laser deposition with in situ heating and post annealing. J Magn Magn Mater 324(18):2894–2898.
3. Masoudpanah SM, Ebrahimi SAS (2012) Synthesis and characterization of nanostructured strontium hexaferrite thin films by the sol–gel method. J Magn Magn Mater 324(14):2239–2244.
4. Wong YC, Wang J, Teh GB (2014) Structural and magnetic studies of SrFe12O19 by sol-gel method. Procedia Eng 76:45–52.
5. Mosleh Z, Kameli P, Ranjbar M, Salamati H (2014) Effect of annealing temperature on structural and magnetic properties of BaFe12O19 hexaferrite nanoparticles. Ceram Int 40(5):7279–7284.
6. Ezhil Vizhi R, Harikrishnan V, Saravanan P, Rajan Babu D (2016) Influence of co-substitution on the structural and magnetic properties of nanocrystalline $Ba_{0.5}Sr_{0.5}Fe_{12}O_{19}$. J Cryst Growth 452:117–124.
7. Li Q, Song J, Saura-Múzquiz M, Besenbacher F, Christensen M, Dong M (2016) Magnetic properties of strontium hexaferrite nanostructures measured with magnetic force microscopy. Sci Rep 6(April):1–7.
8. Pullar RC (2012) Hexagonal ferrites: a review of the synthesis, properties and applications of hexaferrite ceramics. Prog Mater Sci 57(7):1191–1334.
9. Ganjali M, Ganjali M, Eskandari A, Aminzare M (2013) Effect of heat treatment on structural and magnetic properties of Nanocrystalline SrFe12O19 hexaferrite synthesized by co-precipitation method. J Adv Mater Process 1(4):41–48.
10. Lu HF, Hong RY, Li HZ (2011) Influence of surfactants on co-precipitation synthesis of strontium ferrite. J Alloy Comp 509(41):10127–10131.
11. Guo Z-B, Ding W-P, Zhong W, Zhang J-R, Du Y-W (1997) Preparation and magnetic properties of SrFe12O19 particles prepared by the salt-melt method. J Magn Magn Mater 175(3):333–336.
12. Dang TMH, Trinh VD, Bui DH, Phan MH, Huynh DC (2012) Sol–gel hydrothermal synthesis of strontium hexaferrite nanoparticles and the relation between their crystal structure and high coercivity properties. Adv Nat Sci (Nanosci Nanotech) 3(2):25015.
13. Xia A, Zuo C, Chen L, Jin C, Lv Y (2013) Hexagonal SrFe12O19 ferrites: hydrothermal synthesis and their sintering properties. J Magn Magn Mater 332:186–191.
14. Fang J, Wang J, Gan L-M, Ng S-C, Ding J, Liu X (2000) Fine strontium ferrite powders from an ethanol-based microemulsion. J Am Ceram Soc 83(5):1049–1055.
15. Kanagesan S, Hashim M, Jesurani S, Kalaivani T, Ismail I, Ahmod CS (2013) Effect of microwave sintering on microstructural and magnetic properties of strontium hexaferrite using sol-gel technique. J Mater Sci Mater Electron 24(10):3881–3884.
16. Li YL, Feng TF, Chen ZY (2011) Dependence of microstructure and magnetic properties of FePt/B nanocomposite films on boron content. Appl Surf Sci 257(8):3666–3669.
17. Sakka S (2005) Handbook of sol-gel science and technology. 1. Sol-gel processing. Kluwer Academic Publishers, Massachusetts.
18. Sulaiman S, Azis RS, Hassan J, Zakaria A, Muda NNC, Shahrani NMM et al (2015) Effect of pH variation on magnetic properties of strontium hexaferrite. J Solid State Sci Technol Lett 16(1):83–87.
19. Alamolhoda S, Mirkazemi SM, Shahjooyi T, Benvidi N (2016) Effect of pH changes on phase constituents, microstructure and magnetic properties of nano-sized $NiFe_2O_4$ powder synthesized by sol-gel auto combustion method. Iran J Mater Sci Eng 13:21–27.
20. Masoudpanah SM, Seyyed Ebrahimi SA (2011) Effect of pH value on the structural and magnetic properties of nanocrystalline strontium hexaferrite thin films. J Magn Magn Mater 323(21):2643–2647 Elsevier.
21. Hosseini Vajargah S, Madaah Hosseini HR, Nemati ZA (2006) Synthesis of nanocrystalline yttrium iron garnets by sol-gel combustion process: the influence of pH of precursor solution. Mater Sci Eng B Solid State Mater Adv Technol 129(1-3):211–215.
22. >Owens GJ, Singh RK, Foroutan F, Alqaysi M, Han CM, Mahapatra C et al (2016) Sol-gel based materials for biomedical applications. Prog Mater Sci 77:1–79.
23. Muller J, Collomb A (1992) A new representation of the bipyramidal site in the SrFe12O19 M-type hexagonal ferrite between 4.6 and 295 K. J Magn Magn Mater 103(1):194–203.
24. Madani SS, Mahmoudzadeh G, Abedini Khorrami S (2012) Influence of pH on the characteristics of cobalt ferrite powder prepared by a combination

of sol-gel auto-combustion and ultrasonic irradiation techniques. J Ceram Process Res 13(2):123–126.
25. Reza G, Ghasemi A, Saidi A (2014) Enhanced magnetic properties of substituted Sr-hexaferrite nanoparticles synthesized by co-precipitation method. Ceram Int 40(3):4945–4952.
26. Malhotra S, Chitkara M, Sandhu IS (2015) Microwave absorption study of nano synthesized strontium ferrite particles in X band. Int J Signal Process Image Process Pattern Recogn 8(10):115–120.
27. Song F, Shen X, Xiang J, Song H (2010 Mar) Formation and magnetic properties of M-Sr ferrite hollow fibers via organic gel-precursor transformation process. Mater Chem Phys 120(1):213–216.
28. Mali A, Ataie A (2005) Structural characterization of nano-crystalline $BaFe_{12}O_{19}$ powders synthesized by sol–gel combustion route. Scr Mater 53(9):1065–1070 Elsevier.
29. Pereira FMM, Junior CAR, Santos MRP, Sohn RSTM, Freire FNA, Sasaki JM et al (2008) Structural and dielectric spectroscopy studies of the M-type barium strontium hexaferrite alloys ($Ba_xSr_{1-x}Fe_{12}O_{19}$). J Mater Sci Mater Electron 19(7):627–638.
30. Yue Z, Guo W, Zhou J, Gui Z, Li L (2004) Synthesis of nanocrystalline ferrites by sol–gel combustion process: the influence of pH value of solution. J Magn Magn Mater 270(1-2):216–223.
31. Yang FJ, Min JJ, Kang ZW, Tu SY, Chen HB, Liu DG et al (2017) The influence of pH value and composition on the microstructure, magnetic properties of Co-Fe-Al Heusler nanoparticles. Chem Phys Lett 670(3):1–4.
32. Tian L, Xu J, Xiao S (2011) The influence of pH and bath composition on the properties of Ni-Co coatings synthesized by electrodeposition. Vacuum 86(1):27–33.
33. Hesani M, Yazdani A, Abedi Ravan B, Ghazanfari M (2010) The effect of particle size on the characteristics of FeCo nanoparticles. Solid State Commun 150(13-14):594–597.
34. Goldman A (2006) Modern Ferrite Technology. Springer Science and Business Media, Inc., Pittsburgh.
35. Anjaneyulu T, Narayana Murthy P, Rafi SM, Bademiya S, Samuel JG (2013) Effect on magnetic properties of zinc doped nano ferrites synthesized by precursor or method. Int Lett Chem Phys Astron 19:37–43.
36. Srikala D, Singh VN, Banerjee A, Mehta BR (2010) Effect of induced shape anisotropy on magnetic properties of ferromagnetic cobalt nanocubes. J Nanosci Nanotechnol 10(12):8088–8094.
37. Otsuki E, Matsuzawa H (1997) Magnetic properties of $SrO.nFe_2O_3$ powder synthesized by self-combustion process. J Phys IV Colloq 07(C1):C1–323–C1–324.
38. Dadfar MR, Seyyed Ebrahimi SA, Masoudpanah SM (2014) Sol–gel synthesis and characterization of $SrFe_{12}O_{19}/TiO_2$ nanocomposites. J Supercond Nov Magn 28(1):89–94.
39. Nazlan R, Hashim M, Abdullah NH, Ibrahim IR, Ismail I (2012) Influence of milling time on the crystallization, morphology and magnetic properties of polycrystalline yttrium iron garnet. Adv Mater Res 501:324–328.
40. Shafie MSE, Hashim M, Ismail I, Kanagesan S, Fadzidah MI, Idza IR et al (2014) Magnetic M–H loops family characteristics in the microstructure evolution of $BaFe_{12}O_{19}$. J Mater Sci Mater Electron 25(9):3787–3794.
41. Zhang C, Liu X, Rehman KMU, Liu C, Li H, Meng X (2017) Influence of Y^{3+} substitution on the structural and magnetic properties of $Sr_{0.7}La_{0.3}Fe_{11.75-x}Y_xCo_{0.25}O_{19}$ hexagonal ferrites. Appl Phys A Mater Sci Process 123(8):526.
42. Zi ZF, Sun YP, Zhu XB, Yang ZR, Dai JM, Song WH (2008) Structural and magnetic properties of SrFe12O19 hexaferrite synthesized by a modified chemical co-precipitation method. J Magn Magn Mater 320(21):2746–2751.
43. Ali I, Islam MU, Awan MS, Ahmad M, Ashiq MN, Naseem S (2013) Effect of Tb^{3+} substitution on the structural and magnetic properties of M-type hexaferrites synthesized by sol–gel auto-combustion technique. J Alloys Compd 550:564–572.
44. Topal U (2008) Factors influencing the remanent properties of hard magnetic barium ferrites: impurity phases and grain sizes. J Magn Magn Mater 320(3-4):331–335.